Numerical estimation of ultrasonic phase velocity and attenuation for longitudinal and shear waves in polycrystalline materials

Vincent Dorval, Nicolas Leymarie, Alexandre Imperiale, Edouard Demaldent, Pierre-Emile Lhuillier

To cite this version:

Vincent Dorval, Nicolas Leymarie, Alexandre Imperiale, Edouard Demaldent, Pierre-Emile Lhuillier. Numerical estimation of ultrasonic phase velocity and attenuation for longitudinal and shear waves in polycrystalline materials. Ultrasonics, 2025, 148, pp.107517. 10.1016/j.ultras.2024.107517 . cea-04847163

HAL Id: cea-04847163
https://cea.hal.science/cea-04847163v1

Submitted on 18 Dec 2024

Graphical Abstract

Numerical estimation of ultrasonic phase velocity and attenuation for longitudinal and shear waves in polycrystalline materials

Vincent Dorval, Nicolas Leymarie, Alexandre Imperiale, Edouard Demaldent, Pierre-Emile Lhuillier

Highlights

Numerical estimation of ultrasonic phase velocity and attenuation for longitudinal and shear waves in polycrystalline materials

Vincent Dorval, Nicolas Leymarie, Alexandre Imperiale, Edouard Demaldent, Pierre-Emile Lhuillier

- Finite Element Modeling of both longitudinal and shear modes of elastic waves in randomly generated periodic Representative Elementary Volumes of microstructures
- Comparison between numerical results and an analytical model for both longitudinal and shear waves
- Modification of the analytical model, improving agreement with numerical results

Numerical estimation of ultrasonic phase velocity and attenuation for longitudinal and shear waves in polycrystalline materials

Vincent Dorval[a,], Nicolas Leymarie[a], Alexandre Imperiale[a], Edouard Demaldent[a], Pierre-Emile Lhuillier[b]

[a] *Université Paris-Saclay, CEA, List, F-91190, Palaiseau, France*
[b] *EDF R&D, EDF Lab Les Renardières, Département Matériaux et Mécanique des Composants, F-77818, Moret-sur-Loing, France*

Abstract

Finite element computations offer ways to study the behavior of ultrasonic waves in polycrystals. In particular, the simulation of plane waves propagation through small representative elementary volumes of a microstructure allows estimating velocities and scattering-induced attenuation for an effective homogenenous material. Existing works on this topic have focused mainly on longitudinal waves. The approach presented here relies on generating periodic samples of microstructures in order to accommodate both longitudinal and shear waves. After some discussion on the parametrization of the simulations and the numerical errors, results are shown for several materials. These results are compared to an established theoretical attenuation model that has been adapted to use a fully analytical expression of the two-point correlation function for the polycrystals of interest, and to use velocities corresponding to different reference media. Promising comparisons are obtained for both longitudinal and shear waves when using more representative media, obtained through Hill averaging or a self-consistent approach. This illustrates how the numerical method can assist in developing and validating analytical models for elastic wave propagation in heterogeneous media.

Keywords: Ultrasonic, Scattering, Attenuation, Microstructure

---

Email address: `vincent.dorval@cea.fr` (Vincent Dorval)

1. Introduction

Ultrasonic waves that propagate through metals undergo attenuation, which is determined by the properties of both the wave and the metal. In certain ultrasonic inspection scenarios, attenuation poses a limitation. In others, it serves as a valuable tool for characterizing material properties. In both cases there is a keen interest in developing models for the purpose of understanding and predicting attenuation. Scattering due to the differences in elastic properties between grains has been identified as the primary cause of ultrasonic attenuation [1, 2] in metals. These differences are caused by the heterogeneity of orientations of anisotropic grains, and also to heterogeneity of phase in the case of multiphase metals. Many analytical models have been developed over several decades in order to predict attenuation [1, 2, 3, 4, 5, 6]. Due to the complexity of scattering mechanisms, these approaches rely on physical approximations. Experimental comparisons have been performed to validate these models [7, 8]. However, these comparisons suffer from significant uncertainty because the models depend on parameters that can be difficult to quantify experimentally, such as single crystal elastic constants and distributions of grain sizes and orientations. Advancements in computational performances have progressively made it possible to apply Finite Element Methods (FEM) to this problem, first in two and then in three dimensions [9, 10, 11]. FEM simulations allow for model validations with perfectly controlled microstructures. In cases where the approximate models prove inaccurate, FEM results can also be used to introduce corrections [12]. FEM-based characterization has largely been applied to longitudinal waves in studies by various authors [9, 11, 13, 14, 15]. Rayleigh waves have also been considered [16]. The focus of most of these works is on the determination of velocities and attenuation coefficient, although there has also been investigations into the quantification of structural noise [17]. The present communication demonstrates how periodic FEM domains can accommodate both longitudinal (L) and shear (S) waves for the evaluation of their ultrasonic velocities and attenuation. The approach employed relies on generating Representative Elementary Volumes (REV) of a virtual microstructure through Voronoi tessellations. Periodic tessellations matching periodic FEM conditions are generated, making the REV suitable for shear plane wave propagation. Results are compared with Weaver's attenuation model [6], to which a modification is proposed: replacing the Voigt-averaged reference medium with a more representative one, such as a Hill-averaged or a self-consistent medium, shows promising results. An analytical formulation of the spatial correlation function of the Voronoi tessellation is also included in the model. The content of this communication is structured into two main sections. The first section describes methods: it details the different steps of the numerical computation method, as well as the analytical modeling. The second section presents results, and includes analyses of the effect of certain FEM parameters, as well as comparisons between numerical and analytical results.

2. Methods

The three steps of the numerical method are detailed in this section: generation of synthetic microstructures, FEM computations of the propagation of ultrasonic waves, and estimation of the velocities and attenuations. An analytical model which is used for comparisons is also presented. Several aspects of the numerical methods stem from the choice of periodic boundary conditions on the lateral faces. Similar studies have relied on symmetric [13, 18], or periodic [19] boundary conditions to mimic the propagation of plane waves in an infinite volume. Periodic boundary conditions are used here primarily because they can accommodate plane S waves with displacements normal to the propagation direction. They also have other advantages: even for an incident L wave, quasi-L waves travel through the anisotropic grains. Their polarization is not strictly along their propagation direction and could be affected by symmetric boundary conditions [19]. Additionally, symmetric boundary conditions have the drawback of effectively doubling the volume of boundary grains by mirroring them [14], locally changing the grain size distribution. Overall, periodic boundary conditions make it easier to guarantee that the microstructure and the elastodynamic behavior are not skewed at the boundaries. A possible drawback of periodic boundary conditions is that the periodicity induced in the microstructure may affect the simulation results [19]. Such an effect would depend on the width of the domain: section 3.2.2 of this communication shows results obtained for varying domain width, in order to verify that it can be ruled out.

2.1. Synthetic volumes of polycrystalline microstructures

Rectangular cuboids samples are considered as Representative Elementary Volumes (REV) of microstructures. Their dimensions in a Cartesian coordinate system defined by axes $(\mathbf{x}, \mathbf{y}, \mathbf{z})$ are noted (L_x, L_y, L_z). Virtual

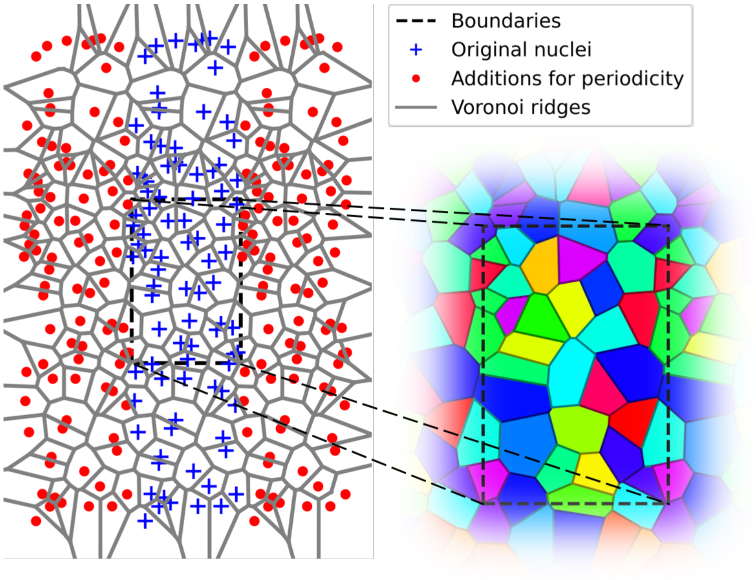

Figure 1: Two-dimensional representation of the periodic microstructure generation procedure. The additions for periodicity are translated copies of the original nuclei. Grain colors indicate crystallographic orientations, showing periodicity in the horizontal direction.

polycrystalline-like microstructures are generated using random Voronoi tesselations. This commonly used method involves randomly placing Voronoi nuclei in the domain [20]. In the present study, the coordinates of Voronoi were independently drawn from uniform distributions. Nuclei are also placed above and below the computation domain in order to ensure that grain statistics are not skewed at the top and bottom boundaries: if these additional nuclei were not added, grains located at these boundaries would tend to occupy a larger volume than others. The entire set of nuclei is duplicated and translated by $-L_x$ and L_x along the $\mathbf{x}$ direction, and the result of this operation is duplicated and translated by $-L_y$ and L_y in the $\mathbf{y}$ direction. This creates periodicity in the $\mathbf{x}$ and $\mathbf{y}$ directions. The procedure is illustrated Figure 1, in two dimensions for better readability.

The crystallographic orientations of each Voronoi region are defined by Euler-Bunge angles (ϕ_1, Φ, ϕ_2). In order to produce an isotropic distribution of orientations, these angles are obtained using the following formula:

$$(\phi_1, \Phi, \phi_2) = (2\pi U_0,\ \arccos(2U_1 - 1),\ 2\pi U_2) \tag{1}$$

where (U_0, U_1, U_2) are three independant random variables following uniform distributions between 0 and 1. Voronoi regions that correspond to duplicated nuclei receive the same orientations as the original ones. This ensures that the elastic properties at the $\mathbf{x}$ and $\mathbf{y}$ boundaries are periodic, as illustrated Figure 1. The nuclei of the full Voronoi tesselation occupy a $3L_x \times 3L_y \times 3L_z$ volume, 27 times larger than the computation domain. The procedure could certainly be optimized in order to provide equivalent results using fewer nuclei. It has also been proposed to save on geometry-related computation costs by reusing grain geometries and only re-randomising crystallographic orientations [19]. However, such optimizations would only yield negligible computation time gains, since the microstructure generation procedure is a relatively fast step of the entire process. The most computationally intensive step is by far the FEM computation itself.

The full computation of the Voronoi tessellation is not actually necessary in the process. Its purpose is to delimit grains in a computation domain. The FEM approach used here only requires the knowledge of elastic properties at a list of points. These properties are determined by the Voronoi regions they belong to. By definition of Voronoi tesselations, a given point is in the Voronoi region of its nearest nuclei. This information can be determined directly from the list of nuclei using a nearest neighbor search, which can be implemented efficiently through a kd-tree algorithm.

2.2. Finite element computations

FEM simulation of ultrasonic propagation through polycrystalline materials can be addressed using structured or unstructured meshes [11]. Structured meshes have the advantage of simplicity, and completely eliminate difficulties that may arise when creating unstructured meshes for potentially problematic geometric features. A structured grid with a regular step in the $(\mathbf{x}, \mathbf{y}, \mathbf{z})$ directions was used in the present study. Let us denote by $\Omega =]0; L_x[\times]0; L_y[\times]0; L_z[$ the domain of interest, and by ϱ and $\mathbf{C}$ the mass density and the elastic constants of the material. Both are space dependent functions, representing the material properties at the scale of the microstructure. Denoting by $\boldsymbol{V}$ the space of admissible displacement fields (typically square integrable fields with square integrable space derivatives), the principle of virtual work satisfied by the exact solution reads: for any time $t > 0$ find $\mathbf{u}(t) \in \boldsymbol{V}$ such that $\forall \mathbf{v} \in \boldsymbol{V}$ we have

$$\frac{\mathrm{d}^2}{\mathrm{d}t^2} \int_\Omega \varrho \mathbf{u} \cdot \mathbf{v} \, \mathrm{d}\Omega + \int_\Omega C\varepsilon(\mathbf{u}) : \varepsilon(\mathbf{v}) \, \mathrm{d}\Omega = \int_{\Gamma_z^+} \mathbf{f}(t) \cdot \mathbf{v} \, \mathrm{d}\Gamma, \tag{2}$$

where Γ_z^+ is the boundary $z = 0$ of the domain. This formulation is completed with null initial conditions. Note that $\mathbf{v}$ is a spatially uniform stress generating a plane wave propagating within the material. This stress is either in the $\mathbf{z}$ or $\mathbf{x}$ direction, depending on whether a L or S wave is to be generated. Traction-free boundary conditions are set on the face $z = L_z$. Periodic boundary conditions are used in the $\mathbf{x}$ and $\mathbf{y}$ directions, matching the periodicity of the Voronoi tessellation described in the previous section. The principle of virtual works can also be expressed as:

$$\frac{\mathrm{d}^2}{\mathrm{d}t^2} m(\mathbf{u}, \mathbf{v}) + k(\mathbf{u}, \mathbf{v}) = \ell(t; \mathbf{v}), \tag{3}$$

where the mass $m(\cdot, \cdot)$ and stiffness $k(\cdot, \cdot)$ bilinear forms clearly appear, while the source term is embedded within the time-dependent linear form $\ell(t; \cdot)$. Denoting by $h = (h_x, h_y, h_z)$ the steps in each direction, we can construct a structured mesh as a regular grid $\mathcal{G}_h$ occupying the domain Ω and made of elements with volume $h_x h_y h_z$. We define ϱ_π and C_π the mass density and the elastic constants approximated as element-wise constant functions. The elastic properties of each element of the grid are set to be those of the grain that the element center falls in. Applying this process leads us to a first approximated problem consisting in finding $\mathbf{u}_\pi(t) \in \boldsymbol{V}$ such that $\forall \mathbf{v} \in \boldsymbol{V}$ we have

$$\frac{\mathrm{d}^2}{\mathrm{d}t^2} m_\pi(\mathbf{u}_\pi, \mathbf{v}) + k_\pi(\mathbf{u}_\pi, \mathbf{v}) = \ell(t; \mathbf{v}), \tag{4}$$

where $m_\pi(\cdot, \cdot)$ and $k_\pi(\cdot, \cdot)$ are the mass and stiffness bilinear forms defined using the projected material parameters on the grid, ϱ_π and C_π respectively. As far as space discretization is concerned, we consider the following conform finite element space:

$$V_h = \{v_h \in \mathcal{C}^0(\overline{\Omega}) \mid \forall K \in \mathcal{G}_h,\ v_h|_K \in Q^1(K)\}, \tag{5}$$

with $Q^1(K)$ the space of polynomial of maximal order one within each element K – note that this actually corresponds to standard basis functions defined at the summits of the grid. We also construct the vectorial counter part of this finite element space $\boldsymbol{V}_h = V_h \times V_h \times V_h$ thus forming a Galerkin approximation of the space $\boldsymbol{V}$. We then seek the (discrete in space) solution $\mathbf{u}_{\pi,h} \in \boldsymbol{V}_h$ such that $\forall \mathbf{v}_h \in \boldsymbol{V}_h$ we have

$$\frac{\mathrm{d}^2}{\mathrm{d}t^2} m_\pi(\mathbf{u}_{\pi,h}, \mathbf{v}_h) + k_\pi(\mathbf{u}_{\pi,h}, \mathbf{v}_h) = \ell(t; \mathbf{v}_h). \tag{6}$$

Finally, we perform a last approximation step, which essentially consists in applying a quadrature formula to evaluate the integrals appearing in the definition of the bilinear forms. We choose an order one formula defined at each summits $\{S_i^K\}_{i=1}^8$ of an element K. More precisely, for any function $f \in \mathcal{C}^0(\overline{\Omega})$, we approximate integrals in the following manner:

$$\int_\Omega f \,\mathrm{d}\Omega = \sum_{K\in\mathcal{G}_h} \int_K f \,\mathrm{d}K \approx \sum_{K\in\mathcal{G}_h} \frac{h_x h_y h_z}{8} \sum_{i=1}^{8} f(S_i^K). \tag{7}$$

Denoting by $m_{\pi,h}(\cdot,\cdot)$ and $k_{\pi,h}(\cdot,\cdot)$ the resulting approximated bilinear forms, we obtain the space discrete problem:

$$\frac{\mathrm{d}^2}{\mathrm{d}t^2} m_{\pi,h}(\mathbf{u}_{\pi,h}, \mathbf{v}_h) + k_{\pi,h}(\mathbf{u}_{\pi,h}, \mathbf{v}_h) = \ell(t; \mathbf{v}_h). \tag{8}$$

As far as time-discretization is concerned, we apply a second-order explicit time scheme, *a.k.a.* the "leap-frog" scheme. Denoting by Δt the time step, and by $t^n = n\Delta t$ any discrete time value such that $\mathbf{u}_{\pi,h}^n$ corresponds to an approximation of $\mathbf{u}_{\pi,h}(t^n)$, the fully-discrete scheme reads:

$$\frac{1}{\Delta t^2} m_{\pi,h}(\mathbf{u}_{\pi,h}^{n+1} - 2\mathbf{u}_{\pi,h}^{n} + \mathbf{u}_{\pi,h}^{n-1}, \mathbf{v}_h) + k_{\pi,h}(\mathbf{u}_{\pi,h}^{n}, \mathbf{v}_h) = \ell(t^n; \mathbf{v}_h), \quad \forall \mathbf{v}_h \in \boldsymbol{V}_h. \tag{9}$$

The time step of the computation is determined by a power iteration method, in order compute the largest eigenvalue appearing in the following expression of the CFL condition:

$$\Delta t \le 2 \Big(\sup_{\mathbf{v}_h \in \boldsymbol{V}_h} \frac{k_{\pi,h}(\mathbf{v}_{\pi,h}, \mathbf{v}_h)}{m_{\pi,h}(\mathbf{v}_{\pi,h}, \mathbf{v}_h)} \Big)^{\frac{1}{2}}. \tag{10}$$

Note that the stiffness term is explicit since it depends on the solution of the previous step. Furthermore, using a quadrature formula whose points match the point of the basis function leads to a diagonal mass matrix – a technique referred to as "mass lumping" in the literature [21, 22]. Thus, the time-marching algorithm only requires to efficiently compute the multiplication of the stiffness matrix times an input vector. In order to increase the performances of this operation, we apply local (*i.e.* at the element level) stiffness matrices in parallel. In terms of memory occupation, the global stiffness matrix is never assembled, and the entries of the diagonal mass matrix are reconstructed "on-the-fly" during the computation. Therefore the memory load of our computations comes solely from storing the three steps $\mathbf{u}_{\pi,h}^{n+1}$, $\mathbf{u}_{\pi,h}^{n}$ and $\mathbf{u}_{\pi,h}^{n-1}$ and the material characteristics ϱ_π and C_π at each grid elements.

2.3. Evaluation of phase velocity and attenuation

The use of plane wave conditions simplifies the evaluation of phase velocity and attenuation. Other approaches use sources with limited dimensions resembling real-life ultrasonic emitters. This adds a need for corrective factors, based on results for the same source in a reference sample [23] for example. In the case of plane waves, two methods have been used to estimate phase velocity and attenuation: a comparison of the field at the upper and lower boundaries [11], or a fit to a series of planes throughout the medium [13]. Only slight differences between the outputs of the two methods have been observed. They were attributed to wave behaviors at the boundaries in the first method [14]. A fit to a series of plane was applied in the present study. It is similar to a method used in a study of ultrasonic propagation through concrete-like microstructures [24]. Its principle is to average the displacement field in a series of horizontal $(\mathbf{x}, \mathbf{y})$ planes, the incident wave propagating vertically along the $\mathbf{z}$ axis. These planes are located at all the $\mathbf{z}$ coordinates of the computation nodes, starting just below the upper boundaries and stopping at a distance from the lower boundary. This buffer distance lets incident wave pass the planes of interest while preventing them from being reflected back. The FEM computation is stopped when the incident wave reaches the lower boundary. The averaged displacement $\mathbf{A}$ is given by:

$$\mathbf{A}(z,t) = \frac{1}{L_x L_y} \int_0^{L_x} \int_0^{L_y} \mathbf{u}(x,y,z,t)\, \mathrm{d}x \mathrm{d}y, \tag{11}$$

$\mathbf{u}$ being the displacement field of the FEM solution. In the following, we are particularly interested in the Fourier transform $\hat{A}(z,\omega)$ of the amplitude in the polarization direction of interest (A_z for L waves, A_x for S waves). The attenuation is then estimated as the slope in a linear regression according to the variable z of the quantity $-\log|\hat{A}(z,\omega)|$. The phase velocity $v(\omega)$ is estimated by maximizing the following quantity:

$$\left| \sum_i \hat{A}(z,\omega) \exp\left(\frac{i\omega z_i}{v(\omega)} \right) \right|. \tag{12}$$

The averaging of $\mathbf{u}$ over $(\mathbf{x}, \mathbf{y})$ aims at approaching the coherent wave, *i.e.* the theoretical average of a wave over all possible realizations of the medium. The limited dimensions of the domain can cause some error. Making the domain larger or averaging $\hat{A}$ over multiple random generations of microstructure would tend to reduce this error. The results presented in this communication are obtained by calculating attenuations and velocities for single realizations of the microstructure in a limited domain, and then averaging them over realizations. This approach has the advantage of easily producing error bars for the velocities and attenuation, based on the variability of estimated values over different realizations. However, averaging $\hat{A}$ over multiple realizations before calculating velocities and attenuation would be more consistent with the theoretical definition of coherent waves. In our experience, performing the average before or after evaluating velocities and attenuation usually yield very similar results. There can be some noticeable differences in specific cases where the variability is very high in the computation domain, for example where they contain very few grains. Such cases are not presented here.

Other authors used time windows around the coherent wave in order to crop out portions of the signal that only consist of incoherent noise [19, 14]. We opted not to apply windowing in this study, in order to avoid the risk of the windows altering the frequency content of the coherent signal. Instead, we aimed at averaging over a sufficient number of realizations to sufficiently reduce the incoherent part of the signal. This approach, while computationally demanding, has the added benefit of reducing incoherent noise even within the time window of the coherent signal, and also simplifying the method and making it more easily reproducible. Illustrative examples of averaging are presented in section 3.1.

2.4. Analytical modeling

We use the Voigt, Reuss, and Hill averages of the medium to provide estimations of the velocities of the coherent waves, and compare them to velocities obtained numerically. Their principles are outlined below. We also apply a more intricate model for obtaining an effective velocity, based on an Eshelby inclusion problem and referred to as the self-consistent approach [25, 26], without discussing its principles in this communication. Numerical attenuation coefficients are compared with those of the analytical model proposed by Weaver [6]. The model consists in solving an equation for the ensemble-averaged Green function, using a first-order smoothing approximation and a Born approximation. The Born approximation causes the model to fail in the geometrical regime, which corresponds to high frequencies where the wavelengths are smaller than grain dimensions. It has however the advantage of yielding a closed form for attenuation coefficients. Other approaches such as the one proposed by Stanke and Kino [5] do not make a Born approximation, and require solving equations numerically to obtain attenuation coefficients. This extends the validity domain of the model to higher frequencies, at the cost of significantly complicating its use and its generalization to other microstructures. Since the frequencies examined in the presented work fall below the geometric domain, the Born-approximated Weaver model is deemed adequate and is applied. The expressions of the attenuation coefficients are summarized later in this section. They assume that the microstructure is statistically isotropic and equiaxed, which is the case of the randomly generated Voronoi tessellations considered in the FEM simulations. This model originally uses the Voigt average as a reference medium, and the effect of replacing some of its parameters by those corresponding to other approaches is evaluated in this communication. The model requires a suitable expression of the two-point correlation function $W(\mathbf{r})$, defined as the probability that two points separated by $\mathbf{r}$ are located in the same grain. A convenient exponential form is often assumed in theoretical developments. However, the exponential form does not describe accurately Voronoi tessellations. A possible solution is to measure empirically the adequate function on generated tessellations. The measured function may optionally be approximated as a sum of exponential functions for convenience [19]. The results presented in this communication rely on an analytical expression of this function, given at the end of this section. Contrarily to the use of velocities from alternative effective media, the use of that correlation function is not a modification of Weaver's models but simply an application to the microstructure geometry considered here.

2.4.1. Voigt, Reuss, and Hill averages of elastic constants for cubic symmetry

The reference effective medium used in attenuation models such as the ones proposed by Weaver and by Stanke and Kino is the Voigt averaged medium. It is obtained under an assumption of uniform strain [27]. An assumption of uniform stress yields another average [28], known as the Reuss average. Hill [29] has shown that the Voigt and Reuss averages provide respectively upper and lower limits for the elastic parameters of a polycrystal, and that the measured values tend to fall close to the middle of the interval. The average of the Voigt and Reuss elastic constants is often referred to as the Hill average. Since the averaged material is isotropic in the untextured case considered here, the elastic constants in the three averages (noted V, R, and H for Voigt, Reuss and Hill) are entirely defined by their terms C^0_{11} and C^0_{44}. C^0_{12} is equal to $C^0_{11} - 2C^0_{44}$. For a polycrystal with cubic single crystal elastic constants noted C_{11}, C_{12} and C_{44}, the averaged values are given by the following expressions:

$$\begin{aligned} C^{0V}_{11} &= \frac{3C_{11} + 2C_{12} + 4C_{44}}{5}, \\ C^{0V}_{44} &= \frac{C_{11} - C_{12} + 3C_{44}}{5}. \end{aligned} \tag{13}$$

$$\begin{aligned} C^{0R}_{11} &= \frac{{C_{11}}^2 + C_{11}C_{12} + 8C_{11}C_{44} - 2{C_{11}}^2 - 4C_{12}C_{44}}{3C_{11} - 3C_{12} + 4C_{44}}, \\ C^{0R}_{44} &= \frac{5(C_{11} - C_{12})C_{44}}{3C_{11} - 3C_{12} + 4C_{44}}. \end{aligned} \tag{14}$$

$$\begin{aligned} C^{0H}_{11} &= \frac{C^{0V}_{11} + C^{0V}_{11}}{2}, \\ C^{0H}_{44} &= \frac{C^{0V}_{44} + C^{0V}_{44}}{2}. \end{aligned} \tag{15}$$

The associated velocities can be obtained based on the averaged elastic constants and the mass density ρ:

$$\begin{aligned} v_L &= \sqrt{\frac{C^0_{11}}{\rho}}, \\ v_S &= \sqrt{\frac{C^0_{44}}{\rho}}. \end{aligned} \tag{16}$$

2.4.2. Attenuation model

Expressions necessary to compute the attenuation are reproduced here, with small changes in notation compared to the original work from Weaver [6]. The attenuation coefficients for L and S waves α_L and α_S are each decomposed as scattering into L and S waves:

$$\begin{aligned} \alpha_L &= \alpha_{LL} + \alpha_{LS}, \\ \alpha_S &= \alpha_{SL} + \alpha_{SS}. \end{aligned} \tag{17}$$

They are given by:

$$\begin{aligned}
\alpha_{LL} &= \frac{\pi^2\omega^4}{2{v_L}^8}\nu^2 \int_{-1}^{1} \eta_{LL}(\theta) L(\theta)\, \mathrm{d}\cos(\theta), \\
\alpha_{LS} &= \frac{\pi^2\omega^4}{2{v_L}^3{v_S}^5}\nu^2 \int_{-1}^{1} \eta_{LS}(\theta) \left[M(\theta) - L(\theta)\right]\, \mathrm{d}\cos(\theta), \\
\alpha_{SL} &= \frac{1}{2}\left(\frac{v_S}{v_L}\right)^2 \alpha_{LS}, \\
\alpha_{SS} &= \frac{\pi^2\omega^4}{4{v_S}^8}\nu^2 \int_{-1}^{1} \eta_{SS}(\theta) \left[N(\theta) - 2L(\theta) + M(\theta)\right]\, \mathrm{d}\cos(\theta).
\end{aligned} \tag{18}$$

ν is the anisotropy factor of the single crystal elastic constants, that are assumed to have a cubic form, normalized by the mass density ρ:

$$\nu = \frac{C_{11} - C_{12} - 2C_{44}}{\rho} \tag{19}$$

L, M, and N correspond to integrals over elastic orientations and scattering directions and are function of the scattering angle θ:

$$\begin{aligned}
L(\theta) &= \frac{9}{525} + \frac{6}{525}\cos^2(\theta) + \frac{1}{525}\cos^4(\theta), \\
M(\theta) &= \frac{24}{525} + \frac{12}{525}\cos^2(\theta), \\
N(\theta) &= \frac{63}{525} + \frac{21}{525}\cos^2(\theta).
\end{aligned} \tag{20}$$

It should be noted that ν, L, M, and N in these expressions stem from the computation of the covariance of elastic properties in a Voigt average framework for cubic crystals. The geometrical properties of the microstructure are described by the two-point correlation function $W(\mathbf{r})$. Its spatial Fourier transform is noted $\tilde{\eta}$ and defined for any vector $\mathbf{q}$ as follows:

$$\tilde{\eta}(\mathbf{q}) = \frac{1}{2\pi}^3 \int W(\mathbf{r}) \exp(-i\mathbf{q}\cdot\mathbf{r})\mathrm{d}\mathbf{r}. \tag{21}$$

It is evaluated for several combinations of modes and for unit vectors $\mathbf{p}$ and $\mathbf{s}$, defined as the directions of propagation and scattering. The results only depends of the angle θ between these two vectors.

$$\begin{aligned}
\eta_{LL}(\theta) &= \tilde{\eta}\left(\frac{\omega}{v_L}\mathbf{p} - \frac{\omega}{v_L}\mathbf{s}\right), \\
\eta_{LS}(\theta) &= \tilde{\eta}\left(\frac{\omega}{v_L}\mathbf{p} - \frac{\omega}{v_S}\mathbf{s}\right), \\
\eta_{SS}(\theta) &= \tilde{\eta}\left(\frac{\omega}{v_S}\mathbf{p} - \frac{\omega}{v_S}\mathbf{s}\right).
\end{aligned} \tag{22}$$

The evaluation of these equations may require numerical integrations if the two-point correlation function W does not have a simple analytical form. The expression for W used in this study is given in the next section. The first-order smoothing approximation made by Weaver is similar to the Keller approximation made by Stanke and Kino: they assume weak heterogeneity of the medium. In the case of untextured single phase polycrystalline media, this translates to assuming a low single-grain anisotropy. An error can therefore be expected in the case of highly anisotropic materials. Huang *et al.* studied this error and suggested correcting it in two ways: first by fitting it to FEM results [12], and later by using an analytical model based on quasi-static velocities [30]. This communication explores another way to address this issue, based on reference media, that also seems to improve model results. The Weaver and the Stanke and Kino models treat polycrystalline materials as a perturbation of a reference homogeneous medium. In both cases, the Voigt-averaged medium is taken as the reference. Kube and Turner [25] proposed an adaptation of the Weaver model to Reuss-averaged, Hill-averaged, and self-consistent reference media. They modified both the velocities and the elastic covariance tensors in the Weaver equation based on these different reference media. The results shown in this communication are obtained by only adjusting the velocities v_L and v_S in equations (18) and (22). This aims at proposing a model that is relatively easy to evaluate and to extend to more intricate microstructures.

2.4.3. Analytical two-point correlation function

The expression of the two-point correlation used here has been developed from the definition of Voronoi tesselations: the probability that two points are located in the same Voronoi region is equal to the probability that the nucleus closest to one point is also the nucleus closest to the other point. This can be expressed as integrals of conditional probabilities [31], based on the distance L from one point to the nucleus and on the cosine x of the angle formed by the two points and the nucleus. The following expression is obtained, with n being the number of Voronoi regions per unit volume:

$$\begin{aligned} W(R) &= 2\pi n \int_{L=0}^{\infty} \int_{x=-1}^{1} L^2 \exp\left(-\frac{\pi n}{3} F(R,L,x)\right) \mathrm{d}L\mathrm{d}x, \quad \text{with} \\ F(R,L,x) &= 2(L^2+R^2-2LRx)^{\frac{3}{2}}+2L^3+3(x^2+1)RL^2-6xR^2L+2R^3. \end{aligned} \tag{23}$$

In statistically isotropic cases such as the ones considered here, W only depends on $R = |\mathbf{r}|$. A dimensionless expression can be obtained by using $Rn^{\frac{1}{3}}$ as the argument. This expression can be pre-computed and stored, to be used for Voronoi tesselations of any density. The expression has been verified by comparing it to the correlation function measured on generated Voronoi tessellations. Figure 2 shows that the results are in agreement. An exponential function is also included to illustrate how it differs.

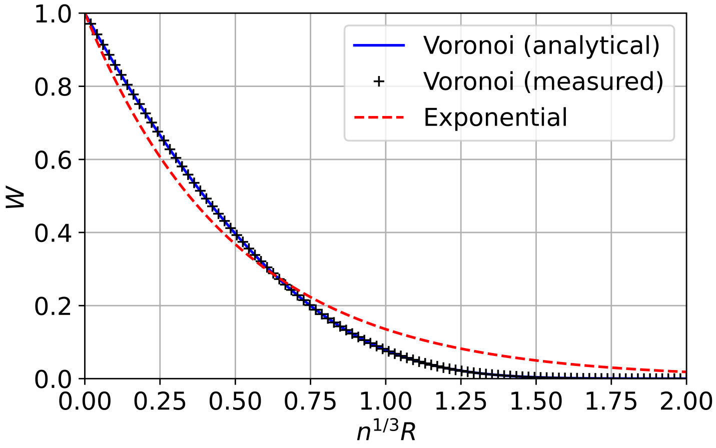

Figure 2: Comparison of the analytical expression of the Voronoi spatial autocorrelation to its empirical measurement on 1000 random locations and directions in 1000 randomly generated Voronoi tessellation, and to an exponential correlation function $\exp\left(-2Rn^{\frac{1}{3}}\right)$.

For practical purposes, using either the analytical or measured function yields equivalent results. However, the analytical form has the advantage of eliminating concerns about measurement accuracy. It could be generalized to other virtual microstructures.

3. Results

3.1. Input parameters

Results are presented for three different materials. Steel, being of particular interest for ultrasonic non-destructive evaluation applications, is the main focus of the study. In order to investigate trends depending on anisotropy, aluminium and lithium are also considered. They have respectively lower and higher anisotropies, and both share similar velocities with steel. The material properties and their source are summarized in Table 1. The Zener ratio Z is a measure of anisotropy in cubic single crystal elastic constants and is given by $Z = \frac{2C_{44}}{C_{11}-C_{12}}$. The velocities that can be derived using the Voigt, Reuss, and Hill averages (noted V, R, and H) and the self-consistent (SC) approach are given in Tables 2 and 3. For all materials, microstructures with n=1000 grains per cubic mm were generated. The cubic root of the average grain volume $n^{-\frac{1}{3}}$=0.1 mm is used here as characteristic grain dimension. Other authors may define grain dimensions in other ways, as there is no unambiguous definition of a single dimension for a distribution of grains with various shapes and sizes.

	ρ ($\mathrm{g\,cm^{-3}}$)	C_{11} (GPa)	C_{12} (GPa)	C_{44} (GPa)	Z
316L steel [32]	7.958	207	133	117	3.16
Aluminum [5]	2.7	103.4	57.1	28.6	1.24
Lithium [12]	0.534	13.4	11.3	9.6	9.14

Table 1: Input material properties of single crystals.

	v_L^V ($\mathrm{m\,s^{-1}}$)	v_L^R ($\mathrm{m\,s^{-1}}$)	v_L^H ($\mathrm{m\,s^{-1}}$)	v_L^SC ($\mathrm{m\,s^{-1}}$)
316L steel	5836	5507	5674	5688
Aluminum	6318	6307	6312	6313
Lithium	6157	5301	5745	5768

Table 2: Longitudinal wave velocities for the Voigt, Reuss, and Hill averages, and for the self-consistent approach.

The dependency with time t for the loads applied at the $z = 0$ boundary is a Ricker wavelet with a characteristic frequency f_0 of 10 MHz. It is defined as follows:

$$\left(2\pi^2 f_0^2 t^2 - 1\right) \exp\left(-\pi^2 f_0^2 t^2\right). \tag{24}$$

	v_S^V ($\mathrm{m\,s^{-1}}$)	v_S^R ($\mathrm{m\,s^{-1}}$)	v_S^H ($\mathrm{m\,s^{-1}}$)	v_S^SC ($\mathrm{m\,s^{-1}}$)
316L steel	3268	2808	3047	3066
Aluminum	3128	3111	3120	3121
Lithium	3402	2055	2810	2845

Table 3: Shear wave velocities for for the Voigt, Reuss, and Hill averages, and for the self-consistent approach.

This time dependency has the advantage of having a sufficiently wide bandwidth to generate results across a range of frequencies around f_0, but it is not essential to the method.

Results will be presented in a frequency band going from 5 MHz to up to 20 MHz. This corresponds to dimensionless wavenumbers $k \cdot n^{-\frac{1}{3}}$ of approximately 0.5 to 2 for L waves and 1 to 4 for S waves. In terms of frequency regimes (or regions) of scattering [5], these ranges should include the transition for the Rayleigh to the stochastic regimes. Attenuation is expected to be proportional to the fourth power of the frequency in the Rayleigh regime and to its square in the stochastic regime. Its behavior in the transition between them is not described by a simple power law, making it interesting for a numerical study.

Slightly different configurations are used for L and S waves. In both cases, the width L_x and L_y are set to 1 mm. The height L_z is 3.5 mm for L waves and 1.75 mm for S waves. This corresponds to similar propagation times for the two waves, as the latter travels at roughly half the speed. The choice of the L_x, L_y and L_z parameters is elaborated upon in sections 3.2.2 and 3.2.3. The calculated field is processed at each of the z coordinates corresponding to nodes in the computation grid, up to z=2.5 mm and z=1.25 mm for L and S waves respectively. Computation domains with examples of microstructure realizations are shown Figure 3. The averages over x and y of the computed displacement as a function of t and z, defined in equation (11) is recorded and stored for post-processing and determination of velocities and attenuations. An example of a cross-section of the computed field and of the averaged displacements is shown Figure 4.

Figure 5 illustrates how the averaging of displacement reduces incoherent noise. In this example, the signal to noise ratio is 12 dB for the local displacement, 34 dB for its average over x and y in a REV, and 44 dB for the average over x and y in 100 REVs.

As explained in section 2.3, results presented below correspond to the

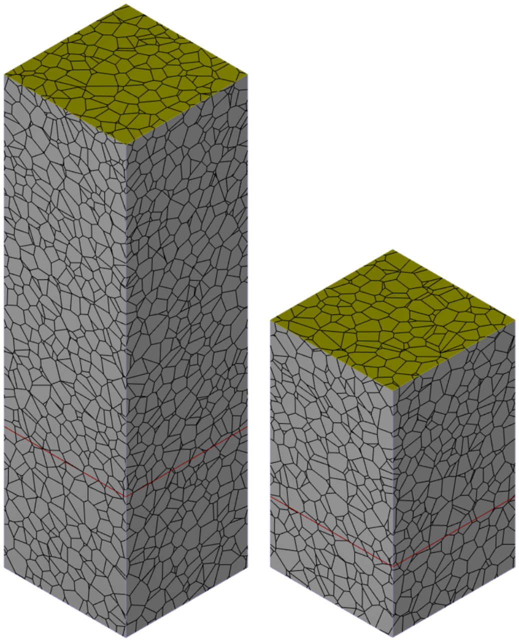

Figure 3: Examples of computation domains for L ($1 \times 1 \times 3.5$ mm, left) and S ($1 \times 1 \times 1.75$ mm, right) waves. The loaded surface (top) is indicated in yellow, and the lower limit of the post-processing zone is indicated by the red line.

averages of velocities and attenuations obtained for signals averaged over individual REVs. In some of them, 95% confidence intervals over a number of microstructure realizations are plotted. Their half-width is given by $\frac{1.960std}{\sqrt{N}}$, where std is the standard deviation over the realizations of the quantity considered (velocity or attenuation), and N the number of realizations.

3.2. Discussion of numerical errors

3.2.1. Grid step

The accuracy of a computation is expected to depend on the number of element compared to relevant scales of the problem. Two scales are to be considered: the ultrasonic wavelengths, and the grain sizes. We performed computations for a homogeneous isotropic material in order to investigate only the relation to wavelength, without involving grains. Figure 6 shows results for a L wave in a material whose velocities were based on the Hill average for steel (see Table 2), with various grid steps. Velocity tends to be underestimated, particularly with increased grid steps and frequency. This

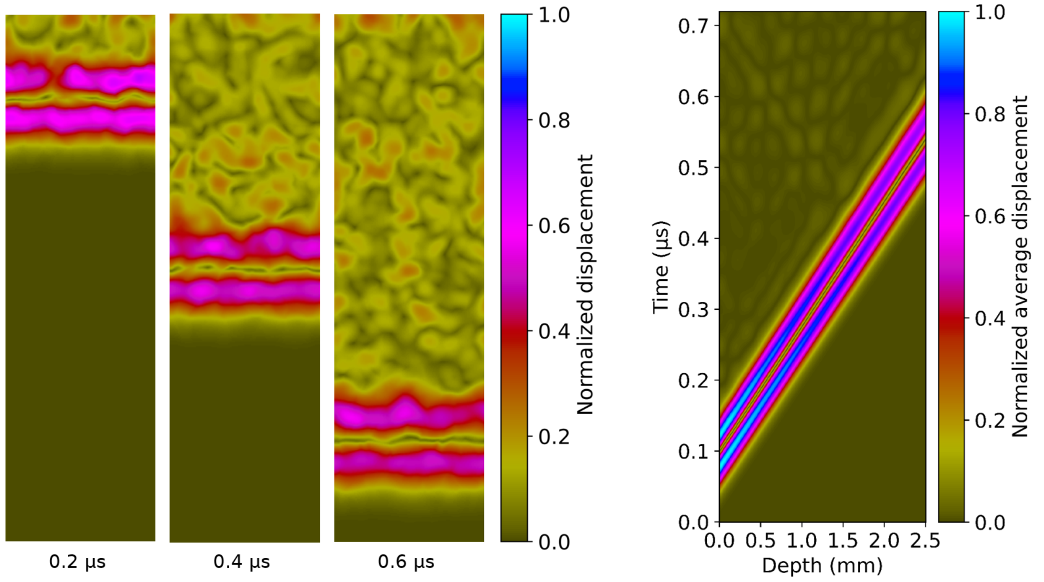

Figure 4: Computed field in a $(\mathbf{x}, \mathbf{z})$ plane, and displacements averaged over $(\mathbf{x}, \mathbf{y})$ planes used in post-processing for a L wave propagating through a steel sample.

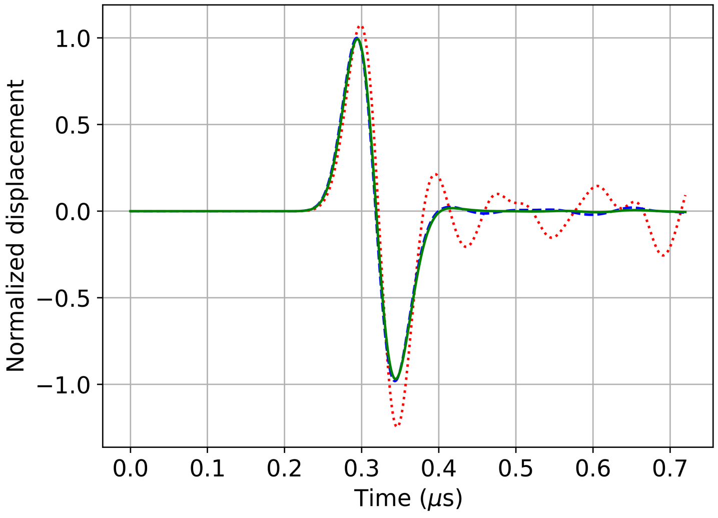

Figure 5: Displacement in the $\mathbf{z}$ direction for an incident L wave in steel: measured locally (··), averaged over$x$ and y for an individual REV (−−), and averaged over x and y for 100 REVs (−).

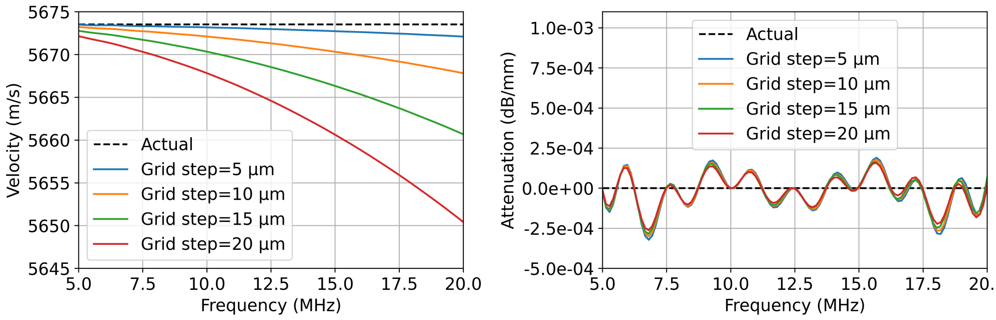

Figure 6: Velocity and attenuation of L waves as a function of frequency in homogeneous Hill-averaged steel with different grid steps.

can attributed to numerical dispersion. The error compared to the actual velocity for the 5 µm grid step is at most 0.02%, and was deemed acceptable. Attenuation is more stable, and the errors observed in its case are small compared to attenuations in polycrystalline metals.

To examine the effect of grid step variations in heterogeneous microstructures, we utilized a consistent set of 20 randomly generated realizations of steel microstructures. For each realization, computations were performed using varying grid steps. The grid step affects not only the FEM scheme, but also the accuracy of the geometrical description of grain boundaries. Large grid steps induce a representation of grains into large voxels. Velocities and attenuations for L waves, averaged over the 20 realizations, are plotted Figure 7.

The behavior observed in the presence of a microstructure differs significantly from that of homogeneous materials: errors are larger, and larger grid steps cause velocity overestimation rather than underestimation. The frequency dependency of the error in velocity is also different. Attenuation also behaves differently compared to the homogenenous case: errors tend to increase in absolute value with frequency, though they remain relatively stable in comparison to the attenuation value itself.

The velocity oscillations as a function of frequency are due to incoherent effects that our approach does not average out for this limited number of realizations. Numerical convergence can still be studied on this set of realizations.

In order to illustrate how numerical errors depend on particular realizations of the microstructure, Figure 8 plots velocities and attenuation at the

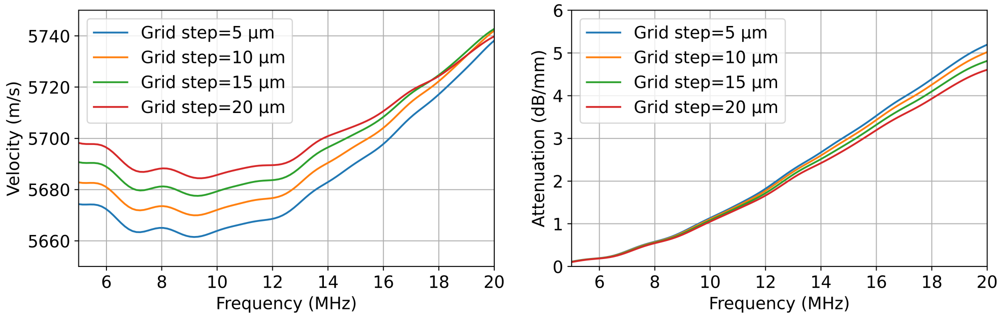

Figure 7: Velocity and attenuation of L waves as a function of frequency for steel microstructures, evaluated numerically and averaged over 20 realizations, with different grid steps.

10 MHz frequency for each of the 20 realizations, with grid steps ranging from 2 to 20 µm. Due to computation times costs, the smallest grid step considered was 2 µm for only two of these realizations, and 4 µm for the others. The number of grid steps is displayed both per Hill-average wavelength λ_{0L} at 10 MHz and per characteristic grain size $n^{-\frac{1}{3}} = 0.1$mm.

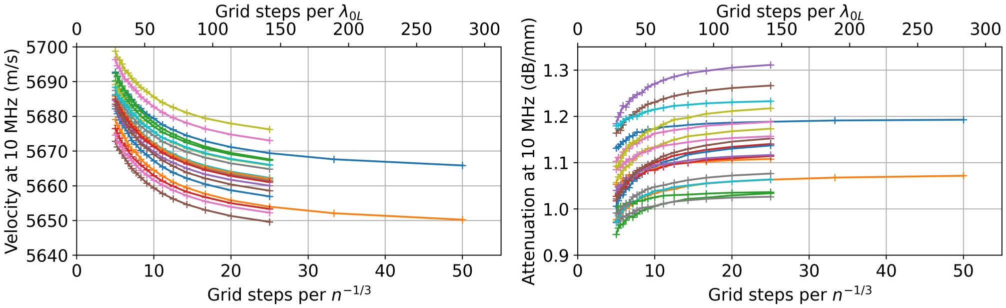

Figure 8: Estimated velocity and attenuation of L waves at 10 MHz as a function of grid resolution for 20 random realizations of steel REVs.

A similar behavior is observed for all realizations: velocity decreases regularly and attenuation increases regularly with grid refinement. This suggests the possibility of estimating errors consistently across numerous realizations based on partial convergence studies, and even correcting for these errors. The convergence observed here does not occur exactly in the same manner as in other studies on similar cases [11]: it could be a consequence of differences in the FEM codes, processing methods, or wavelengths to grain size ratios.

For the computations presented in the following sections, the grid step was set to 5 µm, *i.e* 5% of $n^{-\frac{1}{3}}$ or approximately 20 steps per characteristic grain size. This corresponds to a compromise between computation times and accuracy. With the parameters detailed in the previous subsection, one computation for L waves takes approximately 25 minutes on a computer with a Intel Xeon W-2295 processor and uses at most 8 GB of RAM. The grid step impacts the number of nodes both in space and time, since the time step depends on grid spacing. As a consequence, refining the grid step by a factor 2 multiplies the number of operations in the FEM computations by approximately 16. As Figure 8 illustrates, using more than 20 steps per characteristic grain size would only produce a small change compared to the variability between different random realizations. It is therefore preferable to keep computation times per realization short enough to allow for a significant number of realizations to be processed. For the 5 µm grid step, the time step corresponding to the CFL condition of equation 10 is approximately 0.6 ns.

3.2.2. Width of the domain

The computation method for determining attenuation and velocity requires the computational domain to be representative of the medium. On an intuitive level, it seems that the domain should be wide enough to include a significant number of grains. However, establishing a sufficient width is not straightforward. We performed tests to examine the effect of domain widths. These tests also serve to verify that the periodicity introduced in the sample do not skew results, as such an effect would be expected to depend on width. Figure 9 shows results obtained for three different domain widths. The number of realizations per width was adjusted so that the total volume considered is constant. The grid step is kept at 5 µm in all three cases.

The results obtained for the 1.0 mm and 2.0 mm width are in agreement, with differences falling within their confidence intervals. However, the results for the 0.5 mm width noticeably deviate from them and exhibits significant fluctuations as a function of frequency. We verified that these fluctuations were related to coherent components of the signal that do not average out with additional microstructure realizations. This behavior might be due the domain's width being only 5 typical grain dimensions, skewing the periodic Voronoi tessellations compared to larger domains. This case can therefore not be considered representative of an infinite medium. The results presented

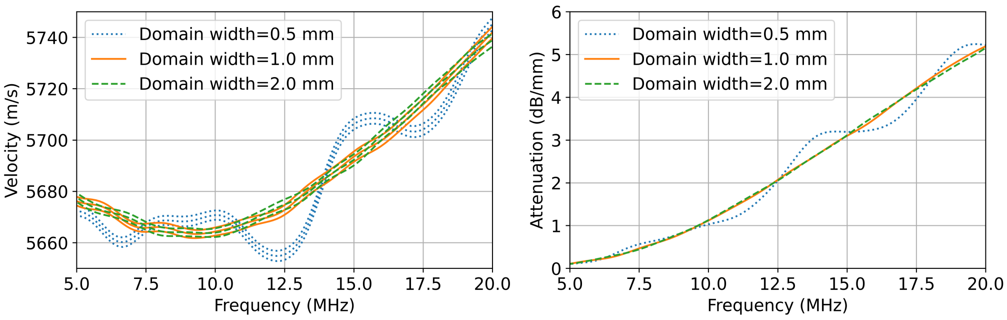

Figure 9: Velocity and attenuation as a function of frequency with 95% confidence intervals, for different domain widths. Results for L waves in steel. 400, 100, and 25 realizations were considered for domain widths 0.5 mm, 1.0 mm and 2.0 mm, respectively.

in the other sections correspond to a 1 mm width with 100 realizations. A 2 mm width with 25 realizations could have been used to produce equivalent results, as the total considered volume would have been the same and the total computation time would have been similar. A potential benefit of using smaller domains with a greater number of realizations is the production of more data for statistical analysis. Additionally, smaller computations have lower requirements in computer memory and are suitable for parallel computing.

3.2.3. Height of the domain

Like the width of the domain, the height affects the number of grains present in the domain and the representativeness of the microstructure. But the estimation of the attenuation poses additional constraints for the choice of this height. A larger height tends to be necessary when attenuation is weak, in order to measure it accurately. Conversely, taller heights may lead to the coherent wave becoming excessively attenuated and falling under the noise, rendering it unusable in post-processing. The choice of the height is therefore heavily dependent on the attenuation, which itself depends on material properties and frequency. The heights employed for the results presented here were chosen empirically as they yielded satisfactory results for the three materials considered. Adjusting this parameter in a more deliberate and optimal manner remains a challenge yet to be addressed.

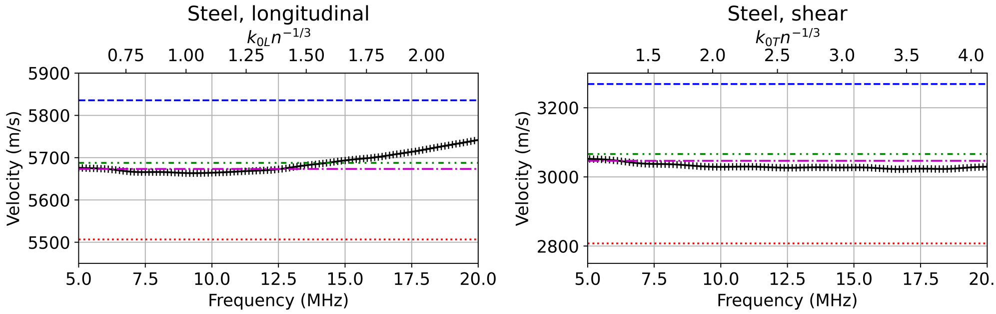

Figure 10: Comparison between Voigt (−−), Reuss (··), and Hill (·−) averages, self-consistent medium (··−), and numerical results (+−) for the velocity as a function of frequency of L and S waves in steel.

3.3. Comparison to an approached analytical model

FEM results are compared to the attenuation model based on Weaver's model [6] with modifications of effective media velocity, detailed in section 2.4. The effective media considered were the Voigt, Reuss, and Hill averages, as well as a self-consistent medium. 100 simulations were performed for each of the three materials (steel, aluminum, and lithium) and each of the two modes (L and S). The velocities for the four effective media and the numerically estimated velocities are shown Figure 10 in the case of steel. Dimensionless wave numbers are indicated for the horizontal axes of figures 10 and 11 in the form $k_{0M}n^{-\frac{1}{3}}$. In this expression, k_{0M} is the wave number for mode M corresponding to the velocity in the Hill average of the material.

The numerically estimated velocities are close to the Hill average and self-consistent velocities. Similar results (not reproduced here) were obtained for aluminum and lithium: the most noticeable difference between materials is the gap between the Voigt and Reuss average velocities compared to the others, as presented in Tables 2 and 3.

Attenuations for aluminum, steel, and lithium (ordered by increasing anisotropy) are shown Figure 11. In most cases, the attenuation is plotted from 5 MHz to 20 MHz. These frequencies correspond to half and twice the main frequency of the emitted 10 MHz Ricker wavelet, and were set as arbitrary boundaries within which usable information was expected to be found. In cases where attenuation is highest, particularly for S waves and for lithium, unexploitable results were obtained at high frequencies and are not included in the plot. This is explained by the amplitude of the coherent wave dropping below the noise threshold over the propagation distance considered here, which prevents from observing its exponential decrease and evaluating its attenuation.

The 95% confidence intervals corresponding to figures 10 and 11 are too narrow to be visible on these plots, and their half-widths at 10 MHz are given in table 4.

	Longitudinal	Shear
Velocities, steel	1.58 $\mathrm{m\,s^{-1}}$	3.22 $\mathrm{m\,s^{-1}}$
Attenuations, aluminium	0.0014 $\mathrm{dB\,mm^{-1}}$	0.0069 $\mathrm{dB\,mm^{-1}}$
Attenuations, steel	0.019 $\mathrm{dB\,mm^{-1}}$	0.095 $\mathrm{dB\,mm^{-1}}$
Attenuations, lithium	0.039 $\mathrm{dB\,mm^{-1}}$	0.55 $\mathrm{dB\,mm^{-1}}$

Table 4: Half-widths of 95% confidence intervals at 10 MHz for the results of figures 10 and 11

These confidence intervals, and numerical errors such as those evaluated Figures 7 and 8, are not expected to significantly affect the comparisons to analytical models. In the case of aluminum, all four versions of the analytical model and the numerical results are in close agreement. The confidence intervals appear to be larger compared to absolute values for this material than for the others. This could be due to the attenuation being weaker in this material, which makes it more difficult to estimate it precisely over the REVs considered here. The differences between the four reference media increase with anisotropy. They are clearly visible for steel, and even more so for lithium. In both cases, and for both L and S waves, the original (Voigt) version of the model seems to underestimate attenuation. An error increasing with anisotropy was expected, as the mathematical development of the model relies on a weak anisotropy approximation. A similar trend has been observed for other models and materials and has been investigated in detail in the case of L waves [30]. Both the Hill and self-consistent versions of the modified attenuation models presented here demonstrate improved agreement with numerical results for the three materials and for both L and S waves. As shown Figure 10, the Hill and self-consistent velocities are also in closer agreement with the numerically observed velocity than Voigt and Reuss. Hence, it would seem logical that substituting the Voigt-averaged velocity with more accurate ones in the attenuation model improves results. But this explanation lacks a rigorous theoretical justification in the framework of Weaver's model. Such theoretical works in this direction would be beyond the scope of the work

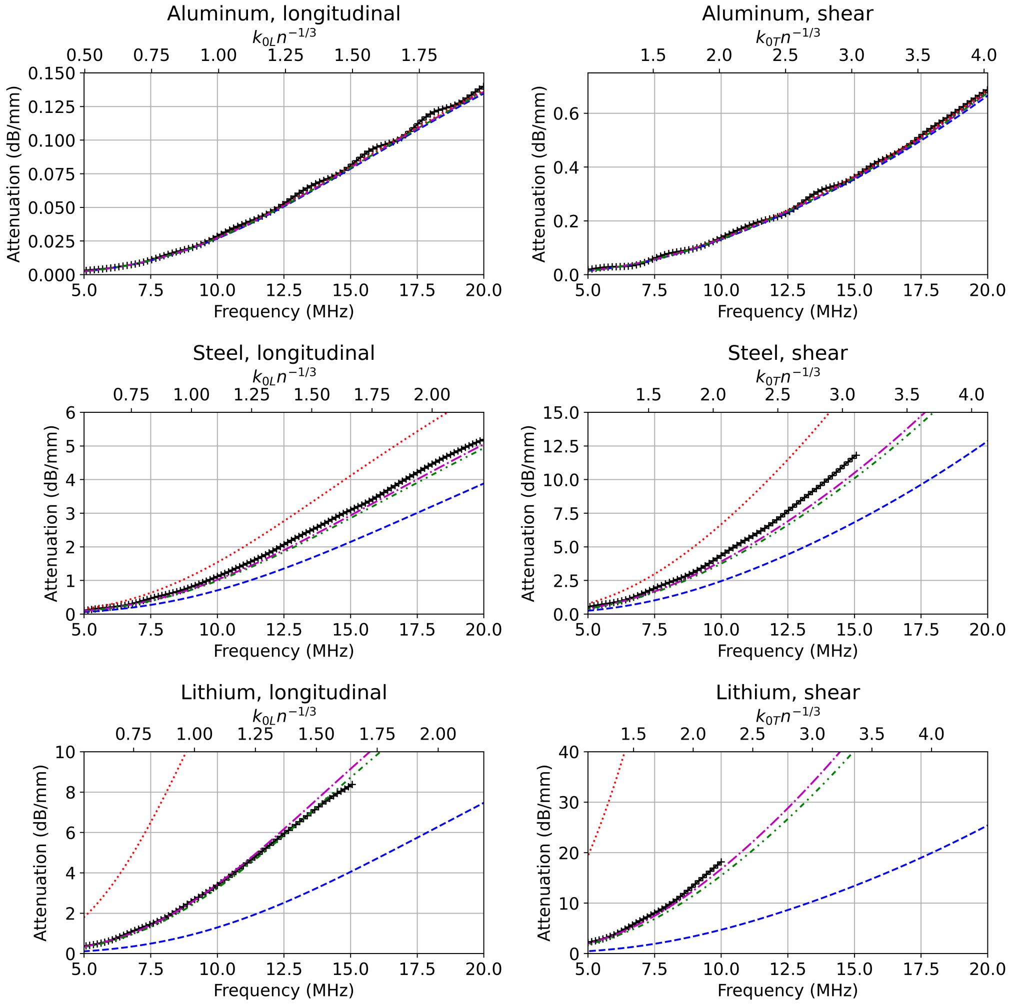

Figure 11: Comparison between numerical (+−) and analytical results for the attenuation as a function of frequency of L and S waves in aluminium, steel, and lithium. Analytical results correspond to the unmodified Weaver model based the Voigt average (−−) and to modifications of the model that use effective velocities from the Reuss average (··), the Hill average (·−), and a self-consistent model (· · −).

presented here. A modification of both the velocities and the elastic covariances has been already suggested [25]. In cases we studied, the modification of the elastic covariance had a small effect compared to the modification of velocities and is not presented here. An alternative self-consistent approach proposed and detailed by the same authors [26] tends to yield an attenuation lower than the one of the unmodified Weaver model and would disagree with our numerical results. Our comparisons do not conclusively determine which of the Hill or self-consistent approach produces the more accurate results. However, given that the more sophisticated self-consistent approach has been demonstrated to be more accurate in velocity measurements [33], it may also be expected to yield a more accurate attenuation model. The main advantage of the Hill average is its ease of calculation, especially for microstructures more complex than the ones studied here. Other ways of obtaining representative values for effective velocities, such as quasi-static analytical models or numerical calculations, could also be considered. And in practical cases, the effective wave velocities in the material of interest are often known through experimental measurements.

The frequency range considered here corresponds to the transition from the Rayleigh to the stochastic regime, which should occur around $k_0 n^{-\frac{1}{3}} = 1$ [5]. Attenuation has been described as power laws of frequency with an exponent of four in the Rayleigh regime and two in the stochastic regime. Exponents evaluated in the case of aluminum, where the exploitable frequency range for shear wave is the largest, are plotted figure 12.

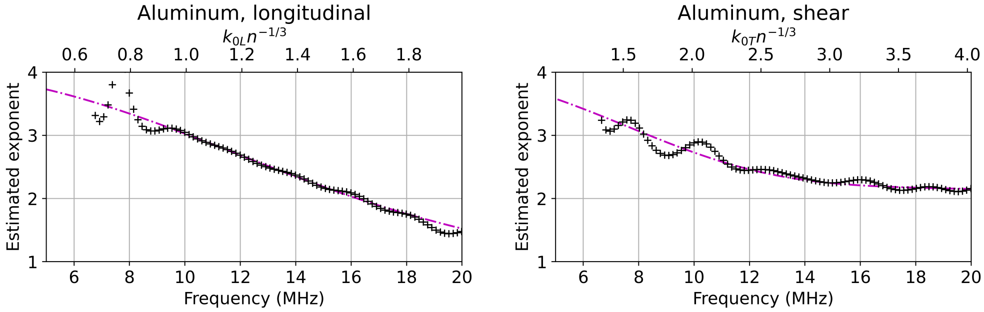

Figure 12: Comparison between the exponent of the numerical results (+−) and of the Hill-modified Weaver model (·−) in the case of L and S waves for aluminum. The exponent is obtained by assuming that the attenuation behaves locally as a power function of the frequency and, in the case of the numerical results, performing a moving average.

Interestingly, the exponents behave differently for longitudinal and shear waves. In both cases it decreases with frequency, but it drops below two for longitudinal waves and not for shear waves. In the results of 11, it translates as a steeper increase at high frequencies for shear waves. The exponent dropping below two for longitudinal waves could appear to contradict expectations for the stochastic regime, but is actually in agreement with modeling results presented by Stanke and Kino [5]. For both aluminum and iron, they shown results where the transition between the Rayleigh and stochastic regimes exhibits a milder slope for longitudinal waves, but not for shear waves. This difference in behavior between longitudinal and shear waves therefore appears to hold across different materials and modeling approaches. Since the transition between the Rayleigh and stochastic regime depends on grain sizes, investigating its relation to grain size distributions could open up possibilities for material characterization.

4. Summary and conclusion

This work contributes to a growing body of research on FEM characterization of ultrasonic wave propagation through polycrystals. The use of periodic boundary conditions associated with the generation of periodic Voronoi tesselations produces virtual polycrystal samples that can accommodate both longitudinal and shear plane waves. After some considerations on the parametrization of the simulations, estimated attenuations for virtual samples of aluminium, steel, and lithium are presented. They are compared to a well-established analytical model, adapted to Voronoi tessellations using a dedicated analytical correlation function, and where the velocities of the reference media are modified. Comparisons to numerical results show a significant improvement in model prediction when its reference velocities are replaced by those of a Hill-averaged or self-consistent medium. These findings apply to both longitudinal and shear waves. The methods outlined in this communication could pave the way for additional research in the numerical characterization of elastic waves, including the frequently overlooked shear waves. The stability of the trends of numerical errors that were observed over multiple microstructure realizations suggest that a multi-fidelity approach could be developed, combining large numbers of low-fidelity FEM simulations to evaluate random variability and a few high-fidelity ones to adjust outcomes. On the topic of analytical models, a more detailed analysis over a wider range of materials would allow determining how robust the improvement provided by the Hill and self consistent approaches are, and whether one produces consistently better results. Alternative effective media and the possible benefits of adjustments to the elastic covariance could also be explored. Such comparisons would be interesting not only for attenuation models but also for velocity dispersion models [34], where effect of modifying the velocity of the reference medium could also be investigated. Although the polycrystalline materials examined in this study had simplistic descriptions as Voronoi tesselations, the same methods can be applied to more intricate and realistic virtual microstructures such as multiphase polycrystals with specific crystallographic orientations. The case of statistically anisotropic textured media requires an adaptation, in order to account for the quasi-longitudinal and quasi-shear natures of the coherent waves. This adaptation is currently being investigated and will be the focus of a future communication.

5. CRediT authorship contribution statement

Vincent Dorval: Conceptualization, Methodology, Software, Formal analysis, Investigation, Visualization, Writing – original draft. **Nicolas Leymarie**: Conceptualization, Methodology, Project administration, Writing – Review & Editing. **Alexandre Imperiale**: Conceptualization, Methodology, Software, Writing – original draft. **Edouard Demaldent**: Supervision, Writing – Review & Editing. **Pierre-Emile Lhuillier**: Project administration, Writing – Review & Editing.

6. Declaration of competing interest

The authors declare that they have no known competing financial interests or personal relationships that could have appeared to influence the work reported in this paper.

References

[1] W. P. Mason, H. J. McSkimin, Attenuation and Scattering of High Frequency Sound Waves in Metals and Glasses, The Journal of the Acoustical Society of America 19 (3) (1947) 464–473. doi:10.1121/1.1916504.

[2] A. B. Bhatia, Scattering of High-Frequency Sound Waves in Polycrystalline Materials, The Journal of the Acoustical Society of America 31 (1) (1959) 16–23. doi:10.1121/1.1907605.

[3] E. P. Papadakis, Grain-Size Distribution in Metals and Its Influence on Ultrasonic Attenuation Measurements, The Journal of the Acoustical Society of America 33 (11) (1961) 1616–1621. doi:10.1121/1.1908517.

[4] S. Hirsekorn, The scattering of ultrasonic waves by polycrystals, The Journal of the Acoustical Society of America 72 (3) (1982) 1021–1031. doi:10.1121/1.388233.

[5] F. E. Stanke, G. S. Kino, A unified theory for elastic wave propagation in polycrystalline materials, The Journal of the Acoustical Society of America 75 (3) (1984) 665–681, number: 3. doi:10.1121/1.390577.

[6] R. Weaver, Diffusivity of ultrasound in polycrystals, Journal of the Mechanics and Physics of Solids 38 (1) (1990) 55–86. doi:10.1016/0022-5096(90)90021-U.

[7] E. P. Papadakis, Ultrasonic Attenuation Caused by Scattering in Polycrystalline Metals, The Journal of the Acoustical Society of America 37 (4) (1965) 711–717. doi:10.1121/1.1909401.

[8] R. B. Thompson, F. Margetan, P. Haldipur, L. Yu, A. Li, P. Panetta, H. Wasan, Scattering of elastic waves in simple and complex polycrystals, Wave Motion 45 (5) (2008) 655–674. doi:10.1016/j.wavemoti.2007.09.008.

[9] G. Ghoshal, J. A. Turner, Numerical model of longitudinal wave scattering in polycrystals, IEEE Transactions on Ultrasonics, Ferroelectrics, and Frequency Control 56 (7) (2009) 1419–1428. doi:10.1109/TUFFC.2009.1197.

[10] B. Chassignole, V. Duwig, M.-A. Ploix, P. Guy, R. El Guerjouma, Modelling the attenuation in the ATHENA finite elements code for the ultrasonic testing of austenitic stainless steel welds, Ultrasonics 49 (8) (2009) 653–658. doi:10.1016/j.ultras.2009.04.001.

[11] A. Van Pamel, C. R. Brett, P. Huthwaite, M. J. S. Lowe, Finite element modelling of elastic wave scattering within a polycrystalline material in two and three dimensions, The Journal of the Acoustical Society of America 138 (4) (2015) 2326–2336. doi:10.1121/1.4931445.

[12] M. Huang, P. Huthwaite, S. I. Rokhlin, M. J. S. Lowe, Finite-element and semi-analytical study of elastic wave propagation in strongly scattering polycrystals, Proceedings of the Royal Society A: Mathematical, Physical and Engineering Sciences 478 (2258) (2022) 20210850. doi:10.1098/rspa.2021.0850.

[13] M. Ryzy, T. Grabec, P. Sedlák, I. A. Veres, Influence of grain morphology on ultrasonic wave attenuation in polycrystalline media with statistically equiaxed grains, The Journal of the Acoustical Society of America 143 (1) (2018) 219–229. doi:10.1121/1.5020785.

[14] M. Huang, G. Sha, P. Huthwaite, S. I. Rokhlin, M. J. S. Lowe, Maximizing the accuracy of finite element simulation of elastic wave propagation in polycrystals, The Journal of the Acoustical Society of America 148 (4) (2020) 1890–1910. doi:10.1121/10.0002102.

[15] X. Bai, B. Tie, J.-H. Schmitt, D. Aubry, Comparison of ultrasonic attenuation within two- and 4 three-dimensional polycrystalline media, Ultrasonics 100 (2020) 105980. doi:10.1016/j.ultras.2019.105980.

[16] T. Grabec, I. A. Veres, M. Ryzy, Surface acoustic wave attenuation in polycrystals: Numerical modeling using a statistical digital twin of an actual sample, Ultrasonics 119 (2022) 106585. doi:10.1016/j.ultras.2021.106585.

[17] X. Bai, B. Tie, J.-H. Schmitt, D. Aubry, Finite element modeling of grain size effects on the ultrasonic microstructural noise backscattering in polycrystalline materials, Ultrasonics 87 (2018) 182–202. doi:10.1016/j.ultras.2018.02.008.

[18] A. Van Pamel, G. Sha, M. J. S. Lowe, S. I. Rokhlin, Numerical and analytic modelling of elastodynamic scattering within polycrystalline materials, The Journal of the Acoustical Society of America 143 (4) (2018) 2394–2408. doi:10.1121/1.5031008.

[19] A. Van Pamel, G. Sha, S. I. Rokhlin, M. J. S. Lowe, Finite-element modelling of elastic wave propagation and scattering within heterogeneous media, Proceedings of the Royal Society A: Mathematical, Physical and Engineering Sciences 473 (2197) (2017) 20160738. doi:10.1098/rspa.2016.0738.

[20] S. Ghosh, Z. Nowak, K. Lee, Tessellation-based computational methods for the characterization and analysis of heterogeneous microstructures, Composites Science and Technology 57 (9-10) (1997) 1187–1210. doi:10.1016/S0266-3538(97)00042-0.

[21] G. C. Cohen, Higher-Order Numerical Methods for Transient Wave Equations, Scientific Computation, Springer Berlin Heidelberg, Berlin, Heidelberg, 2002. doi:10.1007/978-3-662-04823-8.

[22] P. Joly, Numerical Methods for Elastic Wave Propagation, in: M. Destrade, G. Saccomandi (Eds.), Waves in Nonlinear Pre-Stressed Materials, Vol. 495, Springer Vienna, Vienna, 2007, pp. 181–281, series Title: CISM Courses and Lectures. doi:10.1007/978-3-211-73572-5_6.

[23] A. Duijster, A. Volker, F. Van den Berg, C. Celada-Casero, Estimation of Grain Size and Composition in Steel Using Laser UltraSonics Simulations at Different Temperatures, Applied Sciences 13 (2) (2023) 1121. doi:10.3390/app13021121.

[24] T. Yu, J.-F. Chaix, L. Audibert, D. Komatitsch, V. Garnier, J.-M. Hénault, Simulations of ultrasonic wave propagation in concrete based on a two-dimensional numerical model validated analytically and experimentally, Ultrasonics 92 (2019) 21–34. doi:10.1016/j.ultras.2018.07.018.

[25] C. M. Kube, J. A. Turner, Voigt, Reuss, Hill, and self-consistent techniques for modeling ultrasonic scattering, AIP Conference Proceedings 1650 (1) (2015) 926–934. arXiv:https://pubs.aip.org/aip/acp/article-pdf/1650/1/926/16167852/926_1_online.pdf, doi:10.1063/1.4914698.

[26] C. M. Kube, J. A. Turner, Ultrasonic attenuation in polycrystals using a self-consistent approach, Wave Motion 57 (2015) 182–193. doi:10.1016/j.wavemoti.2015.04.002.

[27] W. Voigt, Lehrbuch Der Kristallphysik, Teubner, Leipzig, 1928.

[28] A. Reuss, Berechnung der Fließgrenze von Mischkristallen auf Grund der Plastizitätsbedingung für Einkristalle ., ZAMM - Journal of Applied Mathematics and Mechanics / Zeitschrift für Angewandte Mathematik und Mechanik 9 (1) (1929) 49–58. doi:10.1002/zamm.19290090104.

[29] R. Hill, The Elastic Behaviour of a Crystalline Aggregate, Proceedings of the Physical Society. Section A 65 (5) (1952) 349–354. doi:10.1088/0370-1298/65/5/307.

[30] M. Huang, S. I. Rokhlin, M. J. S. Lowe, Appraising scattering theories for polycrystals of any symmetry using finite elements, Philosophical Transactions of the Royal Society A: Mathematical, Physical and Engineering Sciences 380 (2231) (2022) 20210382. doi:10.1098/rsta.2021.0382.

[31] V. Dorval, Modélisation de la propagation ultrasonore dans une structure métallurgique diffusante, application au CND, Ph.D. thesis, Université d'Aix-Marseille (2009).
URL `https://hal.science/tel-01082035v1`

[32] H. Ledbetter, Monocrystal elastic constants in the ultrasonic study of welds, Ultrasonics 23 (1) (1985) 9–13. doi:10.1016/0041-624X(85)90005-8.

[33] H. M. Ledbetter, Sound velocities and elastic-constant averaging for polycrystalline copper, Journal of Physics D: Applied Physics 13 (10) (1980) 1879–1884. doi:10.1088/0022-3727/13/10/017.

[34] M. Huang, G. Sha, P. Huthwaite, S. I. Rokhlin, M. J. S. Lowe, Elastic wave velocity dispersion in polycrystals with elongated grains: Theoretical and numerical analysis, The Journal of the Acoustical Society of America 148 (6) (2020) 3645–3662. doi:10.1121/10.0002916.